



# Removal of Chromium (VI) and Acid Orange 142 dye from Contaminated Wastewater using Bio-waste Mycelium of *Aspergillus Ustus*: Extraction, Isotherms and Kinetics Studies

L. A. Mohamed<sup>1</sup> · Chukwunonso O. Aniagor<sup>2</sup> · A. A. Aly<sup>3</sup> · A. Hashem<sup>3</sup>

Received: 25 April 2023 / Revised: 30 June 2023 / Accepted: 10 July 2023 / Published online: 21 July 2023  
© The Author(s), under exclusive licence to Springer Nature Singapore Pte Ltd. 2023

## Abstract

This work reported the adsorption of Cr (VI) ions and acid orange 142 dye onto dead fungal biomass. The mycelium of *Aspergillus ustus* (MAU) was successfully cultured, grown, extracted and utilized as an efficient adsorbent. The extensive characterization studies of the as-prepared MAU sample were achieved with the Fourier Transform Infrared Spectrophotometer (FTIR), X-ray diffraction (XRD), Scanning Electron Microscopy (SEM) and Energy Dispersive X-ray (EDX) analyses. Process variables' effects were conducted in the following ranges: pH (3.0–6.0), contact time (0–120 min) and MAU dosage (0.5–5.0 g/L). The FTIR studies revealed that the amino, hydroxyl, and acetamide functional groups on the MAU provided veritable sites for Cr (VI) and AO142 binding. Optimum Cr (VI) uptake was however recorded at 80 min at pH 5.0, while that of AO142 dye was established at 120 min and pH 3.0. The Temkin and pseudo-second-order model aptly described the experimental isotherm and kinetic data. Hence, the MAU was efficient at adsorbing Cr (VI) and AO142 dye from an aqueous solution, but with a higher adsorption capacity for the AO142 molecules.

**Keywords** *Aspergillus ustus* · Hexavalent chromium · Acid orange 142 dye · Adsorption · Fungal biomass

## Introduction

The increased anthropogenic activities and poor wastewater disposal habits have heightened the incidences of heavy metal pollution and its attendant environmental toxicity [1]. The main contributory factor to the toxicity of heavy metals in the aquatic environment lies in their high solubility and bioaccumulation tendencies [2]. Different heavy metals and dye materials constantly find their way into the aquatic environment with severe deleterious consequences. Generally, wastewater from electroplating, refineries, textile dyeing and

leather tanning industries is heavily coloured and also laden with chromium contaminants of different valence states [3].

According to the United States, Environmental Protection Agency (USEPA), the chromium concentration benchmark in drinking water, inland surface water, marine coastal areas and public sewers are placed at 0.05, 0.1, 1.0 and 2.0 mg/L, respectively [4]. According to Asfaw et al. [5], the concentrations of total Cr, Cr(III) and Cr(VI) ranged from 1.24 – 823.87 mg/L, 1.21 – 821.86 mg/L and 0.033 – 2.01 mg/L for tannery wastewater collected from Kombolcha, South Wollo and Ethiopia, respectively. In terms of environmental stability, only the hexavalent chromium [Cr(VI)] and trivalent chromium [Cr(III)] are noteworthy, but the Cr(VI) uptake is emphasized in this study as it depicts much more toxicity [6, 7]. Consumption of Cr(VI) contaminated water can be carcinogenic, mutagenic, and teratogenic to biological systems [8]. Also, increased fish mortality, as well as skin allergies, birth defects, and infertility in humans due to exposure to Cr(VI) has been reported [9, 10]. Similarly, acid orange 142 (AO142) dye as a water-soluble anionic (acid) dye is composed of benzene, nitrobenzene and other aromatic groups [11]. Due to these chemical components, acid orange 142 dye

✉ Chukwunonso O. Aniagor  
co.aniagor@unizik.edu.ng

✉ A. Hashem  
alhashem2000@yahoo.com

<sup>1</sup> Biotechnology Research Institute, National Research Centre, Dokki, Cairo, Egypt

<sup>2</sup> Department of Chemical Engineering, Nnamdi Azikiwe University, P.M.B. 5025, Awka, Nigeria

<sup>3</sup> Textile Research and Technology Institute, National Research Centre, Dokki, Cairo, Egypt

contamination has toxic and mutagenic implications for the aquatic ecosystem [12]. Cases of severe genetic mutilation and rhinitis due to the presence of AO142 dye in the aqueous environment and its subsequent ingestion has been reported [13]. Considering the aforementioned consequences of Cr(VI) and AO142 dye contamination, their efficient detoxification from the aqueous environment is paramount.

The physical and chemical techniques which have been explored for achieving efficient sequestration of both contaminants have some associated limitations [14]. For instance, the electrochemical precipitation technique which showed about 99.0% efficiency for removing Cr(VI) and colour degradation is energy-intensive [4]. Also, the sulphide precipitation approach utilizes expensive reagents and generates secondary effluents [15]. Meanwhile, the adsorption technique using microbial communities is not only efficient but also operationally flexible [16–18].

Fungi, a member of the microbial communities are preferred as potential sources of cheap biosorbent material due to their high surface area and abundant intracellular spaces which are efficient for both heavy metal and organic pollutant sequestration. Both dead and living fungi have a remarkable capacity to take up harmful contaminants from aqueous solutions. However, for a variety of reasons, dead biomass was thought to be preferable to living biomass [19]. The primary contributing factor was the large surface area of the dead cells since the majority of dyestuff binding on fungal biomass occurs via physisorption onto the two-dimensional solid cell wall. On the other hand, were not the best choice for biosorbents due to their small size and weak mechanical strength which often requires substantial hydrostatic pressure to sustain the solute flow rate. The system could be operated at various pH levels and

temperatures, with no deleterious effects on the dead biomass. Additionally, using dead biomass saved money because it eliminated the need for media for fungus growth. Recycling of dead biomass is also possible after regeneration, a development which is far more difficult for live biomass. Sharma et al. [20] studied the adsorption of mercury ( $\text{Hg}^{2+}$ ) ions onto white rot fungus (*Phlebia floridensis*). The post-adsorption sample analyses revealed about 70% – 84% removal efficiency. Three fungal strains were tested for removing Thallium ions from aqueous solutions [21]. The respective fungal strains showed excellent removal performance, with maximum adsorption capacities of 94.69 mg/g, 66.97 mg/g, and 52.98 mg/g for *Fusarium sp.*, *Arthrimum sp.*, and *Phoma sp.*, respectively. Also, *Scopulariopsis brevicompactum* [22] and *Aspergillus terricola* [6] were isolated and respectively explored for Pb (II) and Cr (VI) adsorption. However, optimal heavy metal uptake was achieved in both studies. Almeida and Corso [23] adsorbed acid blue 161 and procion red MX-5B dyes on the fungi *Aspergillus niger*, *Aspergillus terreus* and *Rhizopus oligosporus* biomasses. The fungal biomass demonstrated good adsorption capacity, with efficient toxicity elimination. This study explored the adsorptive potentials of mycelium from *Aspergillus Ustus* (MAU) towards aqueous AO142 dye and Cr (VI) ions in a batch system.

## Materials and Methods

### Materials

The *Aspergillus ustus* strain was obtained from the culture collections of the Department of Microbial Chemistry, National

**Scheme 1** Presentation of the different processes involved during the adsorbent synthesis

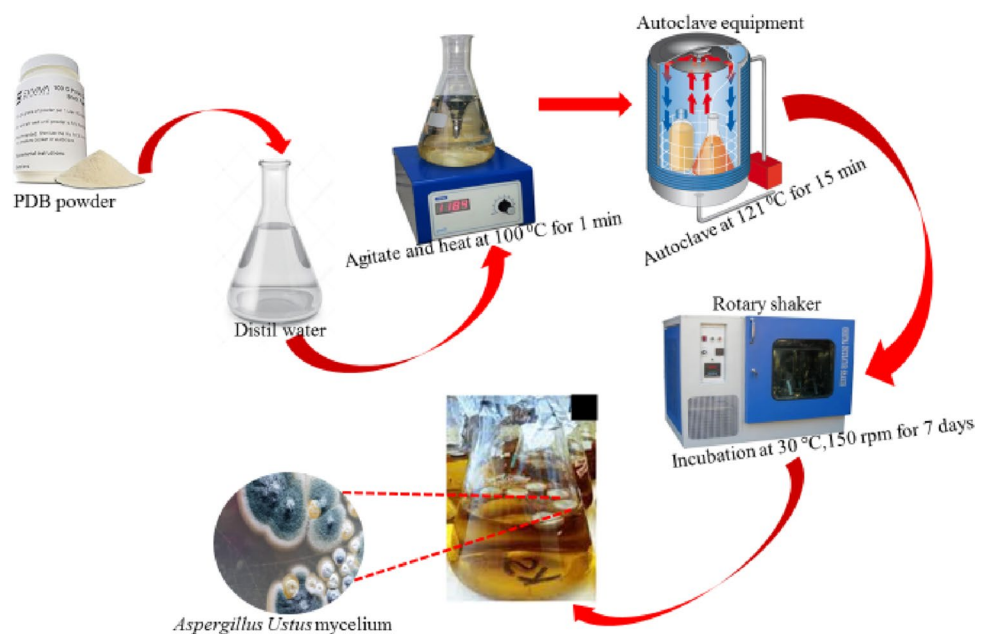


**Table 1** The isotherm model equations applied in the study

Isotherm models	
2-parameter models	
Langmuir	$q_e = \frac{q_m k_L C_e}{1 + k_L C_e}$
Freundlich	$q_e = K_F (C_e)^{\frac{1}{n_F}}$
Tempkin	$q_e = \frac{RT}{b_T} \ln(K_T C_e)$
Kinetic models	
Pseudo-first-order (PFO)	$q_t = q_e [1 - \exp(-k_1 t)]$
Pseudo-second-order (PSO)	$q_t = \frac{k_2 q_e^2 t}{1 + k_2 q_e t}$
Bangham	$q_t = q_e [1 - \exp(-k_b t^n)]$
3-parameter models	
Hill	$q_e = \frac{q_{mH} C_e^{n_H}}{K_H + C_e^{n_H}}$
Sip	$q_e = \frac{K_S C_e^{\beta_1}}{1 + a_S C_e^{\beta_1}}$
Toth	$q_e = \frac{k_T C_e}{(a_T + C_e)^n}$

[ $a_T$ , Toth isotherm constant (L/mg);  $b_T$ , Temkin constant that is related to the adsorption heat (J/mol);  $k_1$ , Pseudo-first-order rate constant (1/min);  $k_2$ , Pseudo-second-order rate constant (g/mg<sup>2</sup> min);  $K_F$ , Freundlich isotherm constant [(mg/g) (L/mg)<sup>1/n<sub>F</sub></sup>];  $K_L$ , Langmuir constant (L/g);  $K_T$ , Temkin initial adsorption rate (mg/(g min));  $n_F$ , Freundlich adsorption intensity;  $R$ , Universal gas constant (8.314 J/Kmol);  $R_L$ , Langmuir's dimensionless constant (separation factor);  $T$ , Temperature (K);  $q_{max}$ , maximum adsorption capacity (mg/g);  $K_S$ , Sips isotherm model constant (L/g);  $\beta$ , is Sips isotherm exponent;  $a_S$ , Sips isotherm model constant (L/g);  $K_S$ , Sips isotherm model constant (L/g);  $n_H$ , Hill cooperativity coefficient of the binding interaction;  $q_{mH}$ , Hill isotherm maximum uptake saturation (mg/L);  $K_H$ , Hill isotherm constant,  $K_b$ , Bangham model constants;  $n$ , Bangham model exponent]

Research Center, Dokki, Cairo, Egypt. The following reagents used in the study: Potassium dichromate from Sigma-Aldrich (Brno, Czech Republic), sodium hydroxide, sodium carbonate, nitric acid, HCl, ethyl alcohol, and acetone were laboratory-grade chemicals (Merck, Germany).

**Preparation of Growth Medium for Mycelium Extraction**

Suspend 26.5 g of PDB powder in 1 L of deionized water, then the solution was heated to 100 °C until completely dissolved. The obtained solution was sterilized at 121 °C for 15 min in an autoclave. The growth medium was studied in conical flasks containing PDB medium (50 ml). Cultures were incubated on a rotary shaker at 30 °C and 150 rpm for up to 7 days. Mycelium was removed from the media by filtration. The protocol for extracting the mycelium is detailed in our previous work [6] and schematically illustrated in Scheme 1.

**Batch Adsorption Studies**

The equilibrium and kinetic experimental procedures have been reported previously [24]. The experiment was conducted at the following reaction conditions: MAU dosage, 0.2 g/L; initial Cr (VI) and AO142 dye concentration, 10–100 mg/L; temperature, 30 °C; stirring speed, 200 rpm; contact time, 0–180 min. The Cr (VI) and AO142 dye concentrations in the supernatant solution were respectively determined by the diphenyl carbazide method [25] and on a Shimadzu UV/Visible Spectrophotometer at ~480 nm wavelength. The amount of the respective pollutants

adsorbed at each instant ( $q_t$ , mg/g) and equilibrium ( $q_e$ , mg/g) is evaluated from Eqs. (1) and (2), respectively.

$$q_t = \frac{(C_o - C_t) * V}{W} \tag{1}$$

$$q_e = \frac{(C_o - C_e) * V}{W} \tag{2}$$

where  $C_o$  (mg/L),  $C_e$  (mg/L) and  $C_t$  (mg/L) are the initial, equilibrium and instantaneous adsorbate concentrations, respectively.  $V$  (L) is the volume of adsorbate solution used and  $W$  (g) is the mass of the adsorbent.

**Mathematical and Theoretical Backgrounds of the Studied Models**

The mathematical expression of the different models adopted in this study is shown in Table 1. The theoretical basis and fundamental assumptions of the respective models are briefly highlighted herein. Fundamentally, the PFO model postulates that  $\frac{dq_t}{dt} \propto (q_e - q_t)$ . Where  $\frac{dq_t}{dt}$  and  $(q_e - q_t)$  are solute uptake rate and amount of solute adsorbed at equilibrium and at any given time during the process. The PSO model assumes the vacant site occupation follows a second-order rate [26]. The Bangham model assumes an intra-diffusion [27] and thus implies the predominance of solute diffusion into adsorbent pores under conditions of uniform chemical composition [28].

The Langmuir and Freundlich equations describe solute adsorption onto homogenous and heterogenous surfaces

while the Temkin equation describes the variations in adsorption energy mostly for chemisorption [29]. The Hill, Sips and Toth models are 3-parameter isotherms based on Langmuir and Freundlich model characteristics. Specifically, the Hills model explains solute binding onto homogeneous substrates as a cooperative monolayer binding onto non-uniform sites of the same adsorbent [30]. The cooperative phenomenon implies that solute binding on one site could influence the energy and stability of the other sites on the same adsorbent. The Sip model is an upgraded form of the Freundlich model [29]. The model exhibits either Freundlich or Langmuir model characteristics based on the concentration of the adsorbate. The Toth model postulates uneven distribution of adsorption energy between the sorption sites of an adsorbent [31].

### Error Analysis

The fitting goodness of nonlinear models is generally determined using specialized error models. Table 2 presents the mathematical expression of the different error models adopted in the study. Meanwhile, by applying different error models, varying error values were also generated. Hence, to ensure a holistic model analysis, these error values were normalized following the procedure we previously reported [32, 33] to generate the sum of normalized error (SNE) values.

### Instrumental and Physicochemical Characterization Procedures

The FTIR measurements were conducted on a PerkinElmer spectrophotometer within the 4000 to 400  $\text{cm}^{-1}$ , while the SEM and EDX results were respectively determined on a scanning electron microscope (model JEOL-JSM-5600) and

EDX spectrometer (Oxford Instruments 6587 EDX detector). The XRD patterns were obtained on a PAN analytical diffractometer (X'Pert PRO) within the reading range of 2 to 80°. The point of zero charge was determined following the mass titration approach [34]. The Brunauer–Emmett–Teller (BET) surface area measurement was achieved via the nitrogen gas adsorption–desorption method on an automated Belsorp Max surface area analyzer (MicrotracBEL Corp., Japan) at an adsorption temperature of 77 K. A precise mass of the PSP sample was measured and recorded before the analyses. Likewise, the sample underwent additional degassing for 2 h at 200 °C.

## Results and Discussions

### Characterization Results

#### Fourier Transform Infrared Spectroscopic (FTIR) Analysis

Figure 1 shows the FTIR spectra of the native MAU (before adsorption), as well as those after the adsorption of Cr (VI) and AO142 molecules. The raw MAU shows a broad peak around 3260  $\text{cm}^{-1}$ , a characteristic band of all polysaccharides which represents the OH and NH groups. The peak around 2933  $\text{cm}^{-1}$  is due to the symmetric stretching of the  $-\text{CH}_2$  group of both chitin and glucan [35–37]. Also, both peaks at 1639 and 1541  $\text{cm}^{-1}$  are related to the free amino and amide groups in the chitin/chitosan component of the MAU. The single peak at 1639  $\text{cm}^{-1}$  is further evidence that the MAU contains  $\beta$ -linkage of chitin units. The sharp peak recorded around 1020  $\text{cm}^{-1}$  corresponds to the C–O–C of chitin and glucan parts of the MAU [38].

The post-adsorption spectra were mostly characterized by either positive or negative adjustments in the intensity of the peaks involved in the sorption process. For instance, the intensity of peaks assigned to the  $-\text{NH}$  (3360  $\text{cm}^{-1}$ ),  $-\text{OH}$  (3294  $\text{cm}^{-1}$ ), and aliphatic C–H (2900–2800  $\text{cm}^{-1}$ ) slightly diminished. The peak of the primary and secondary amines located between 1660 to 1500  $\text{cm}^{-1}$  also diminished due to the deprotonation of the Lewis basicity of  $-\text{NH}$  and  $-\text{NH}_2$  by the Lewis acidic nature of Cr (VI) and N-heterocyclic nitrogen of the AO142 dye [39]. Furthermore, the intensity reduction of the C–O–C peak at 1025  $\text{cm}^{-1}$  confirms a successful Cr binding onto the MAU.

#### X-ray Diffraction (XRD) Analysis

The X-ray diffraction studies reveal changes in the structural integrity of the adsorbent sample. The spectra of native MAU show a broad  $2\theta$  peak between 15–25°. Such observation is an indication of the amorphous nature of the MAU (Fig. 2). The specific peaks appeared at  $2\theta = 8.9^\circ$  and

**Table 2** Mathematical expression of the error models

Error Function	Equation	Eq. no
ARE	$\sum_{i=1}^n \left  \frac{q_{e,exp} - q_{e,cal}}{q_{e,exp}} \right $	(3)
APE	$\frac{\sum_{i=1}^n  (q_{e,exp} - q_{e,cal})/q_{e,exp} }{N} * 100$	(4)
ERRSQ	$\sum_{i=1}^n [q_{e,cal} - q_{e,exp}]^2$	(5)
Hybrid	$\frac{100}{n-p} \sum_{i=1}^n \left[ \frac{(q_{e,exp} - q_{e,cal})^2}{q_{e,exp}} \right]$	(6)
MPSD	$100 * \sqrt{\frac{1}{n-p} \sum_{i=1}^n \left[ \frac{(q_{e,exp} - q_{e,cal})^2}{q_{e,exp}} \right]}$	(7)
$\chi^2$	$\sum \frac{(q_{e,exp} - q_{e,cal})^2}{q_{e,exp}}$	(8)
$R^2$	$\frac{\sum (q_{e,cal} - q_{e,exp})^2}{\sum (q_{e,cal} - q_{e,exp})^2 + \sum (q_{e,exp} - q_{e,cal})^2}$	(9)

$n$  = number of data points,  $p$  = number of the model parameter

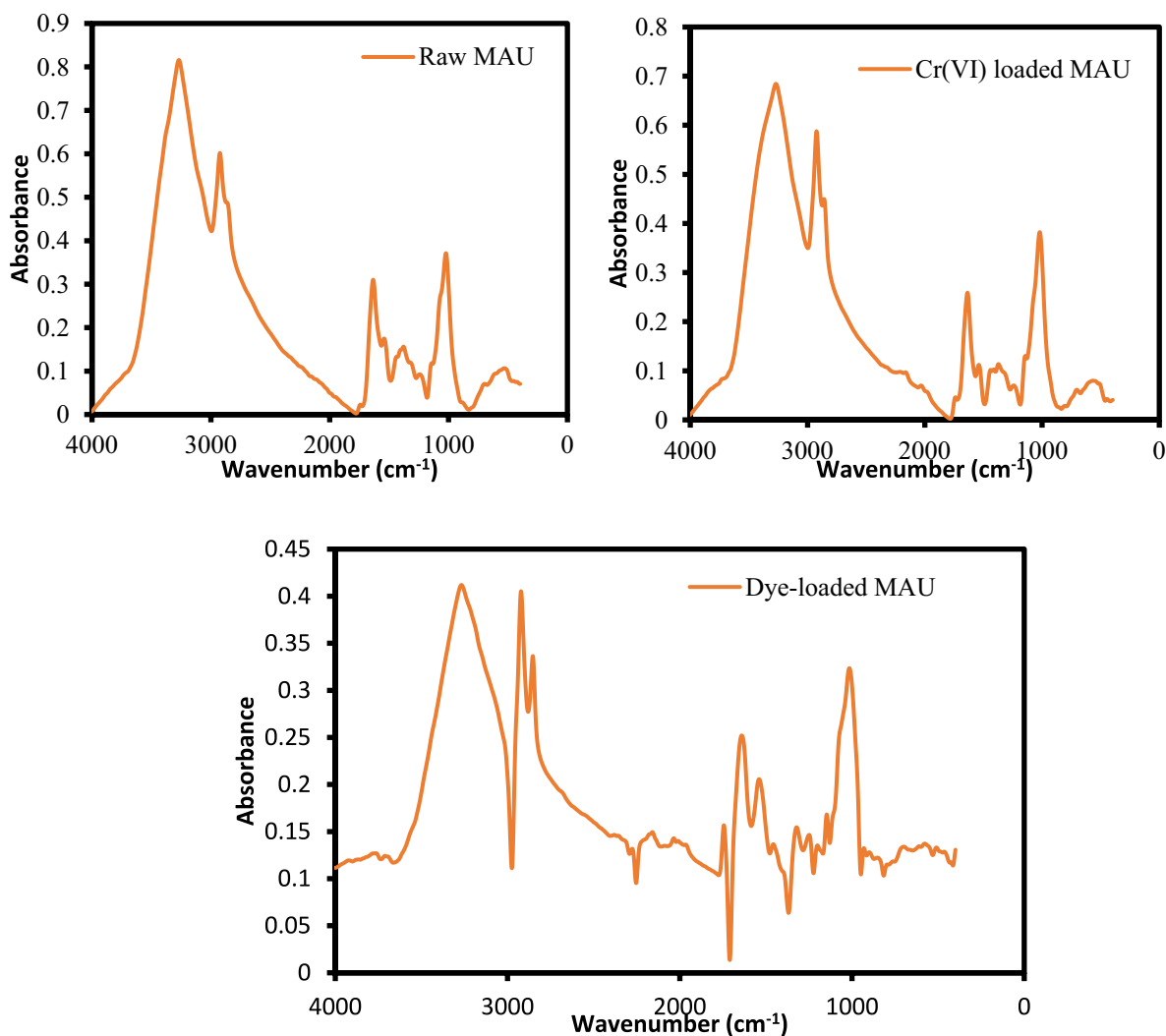


**Fig. 1** FTIR spectra of raw *MAU*, and Cr(VI) loaded *MAU* and dye-loaded *MAU*

19.8°, corresponding to the 020, and 110 planes, respectively. These two representative peaks are related to chitin polymorphs. The crystallinity of the  $\beta$ -glucan component of the *MAU* is responsible for both miniature peaks observed at  $2\theta = 6.3^\circ$  and  $7.5^\circ$ . In both post-adsorption spectra, the relative intensity increased substantively. This is due to the incorporation of respective adsorbates onto the *MAU* surface via electrostatic interaction and/or further chelation with the surface functional groups, such as amino, hydroxyl, and acetamide. Small intensity peaks at  $2\theta = 44.7^\circ$  and  $72.7^\circ$  corresponding to the residual traces of proteins inherent on the *MAU* surface were still retained. Consequently, the absence of any significant changes in the XRD spectra pattern after adsorption suggests a physical adsorption process, where the chemical composition of the adsorbent remains unaltered after adsorption.

### Scanning Electron Microscopy (SEM)

Figure 3(a-b) shows the SEM images of the *MAU* before and after the adsorption process. It was observed that the native (raw) *MAU* shows a rough, compact and flake-like structure with short nanofibril morphology (Fig. 3a). The nanofibril structure is attributed to the strong -OH bonding which exists within chitin and glucan components [36]. After the adsorption process (Fig. 3b), the surface of the *MAU* disbanding into a more individual nanofibril structure. The surface morphology completely changed into more distinguished flakes due to electrostatic interaction and/or chelation of the Cr(VI) cation and AO142 molecules with the surface functional groups of *MAU* (amino, hydroxyl, and acetamide). The aggregate particles marked out in a white square shape on the post-adsorption images in Fig. 3(b & c)

are respectively attributed to some adsorbed chromium ions and AO142 molecules.

### Energy Dispersion X-ray (EDX)

The EDX elemental distribution mapping of the raw *MAU*, Cr(VI)@*MAU* and dye-loaded *MAU* are shown in Table 3, while the mapping spectra of the Cr(VI)@*MAU* and dye-loaded *MAU* are shown in Fig. 4. By comparing the % elemental distribution and EDX spectrum of the unloaded and Cr(VI)-loaded *MAU*, obvious Cr spectra spikes are evident (Fig. 3c). Hence, a successful Cr (VI) adsorption onto the *MAU* surface is concluded. Also, a respective increase and decrease in the %wt of oxygen and carbon compared to that of the raw *MAU* suggest the involvement of oxygen and carbon-based functional groups during adsorption.

For the dye-loaded *MAU*, unlike in the case of the Cr(VI)-loaded *MAU*, the %wt of oxygen and carbon atoms both decreased. Also, a relatively high %wt S and N contents, which are obvious constituents of the AO142 dye, in the dye-loaded *MAU* further suggests successful dye adsorption.

### Surface Area Analyses

According to the findings, *MAU* has specific surface areas and pore sizes of 254.376 m<sup>2</sup>/g and 1.654 nm, respectively. Meanwhile, the BET surface area measurement for fairly porous (micro-, meso-, and macroporous) materials is

thought to have limitations because of its false presumptions [40]. As a result, the surface area measurement technique made popular by Barrett, Joyner, and Halenda (BJH) was also looked into (Table 4). The pore radius determined in this study by the BET and BJH measurement techniques is therefore smaller than 2 nm, which is classified as microporosity according to the IUPAC [41, 42].

### Point of Zero Charge (pHpzc) Analysis

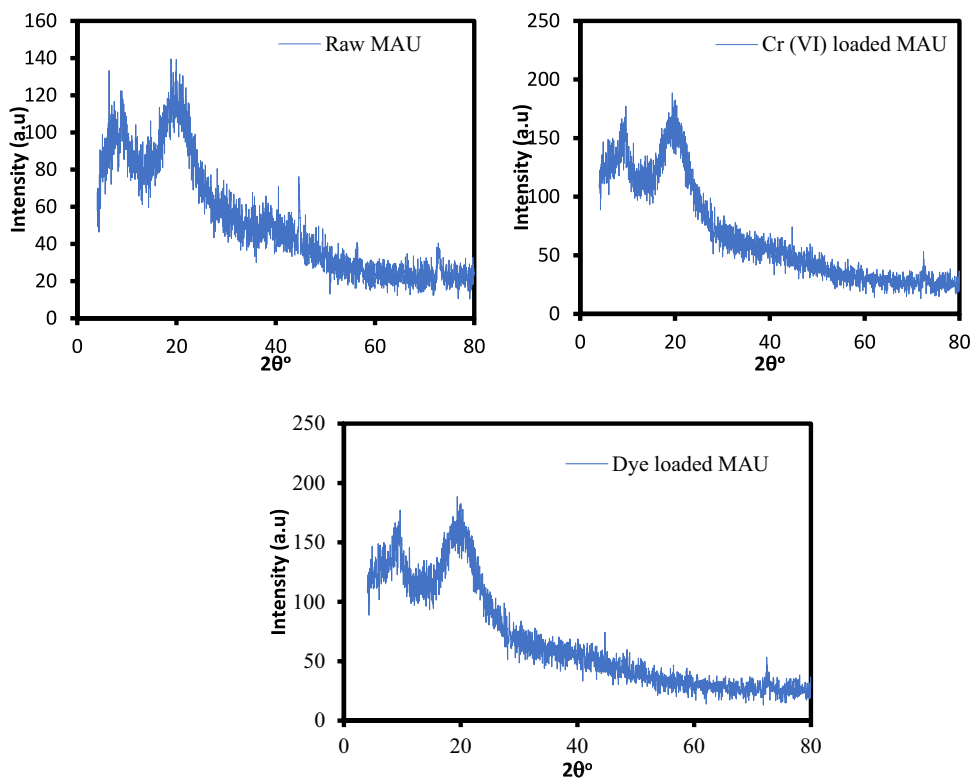
pHpzc is another property that helps in understanding the adsorption reaction mechanism of Cr(VI) onto the *MAU* surface. Generally, for an electrostatically driven adsorption process, the cation uptake occurs mostly at pH > pHpzc, whereas anion adsorption preferential occurs at pH < pHpzc. The pHpzc for the *MAU* sample was recorded at pH 6.2 as shown in Fig. 5, hence, the optimal adsorption of negatively charged chromate ions and AO142 anionic species is expected to occur at lower pH values (pH < pHpzc). Note, the terms: pH<sub>i</sub>, pH<sub>f</sub> and ΔpH denote initial, final and change in liquid pH.

### Adsorption Performance

#### Effect of Solution pH

Solution pH is an important criterion during the adsorption of cationic species, especially in the case of

**Fig. 2** XRD spectra of raw *MAU*, Cr(VI) loaded *MAU* and dye-loaded *MAU*



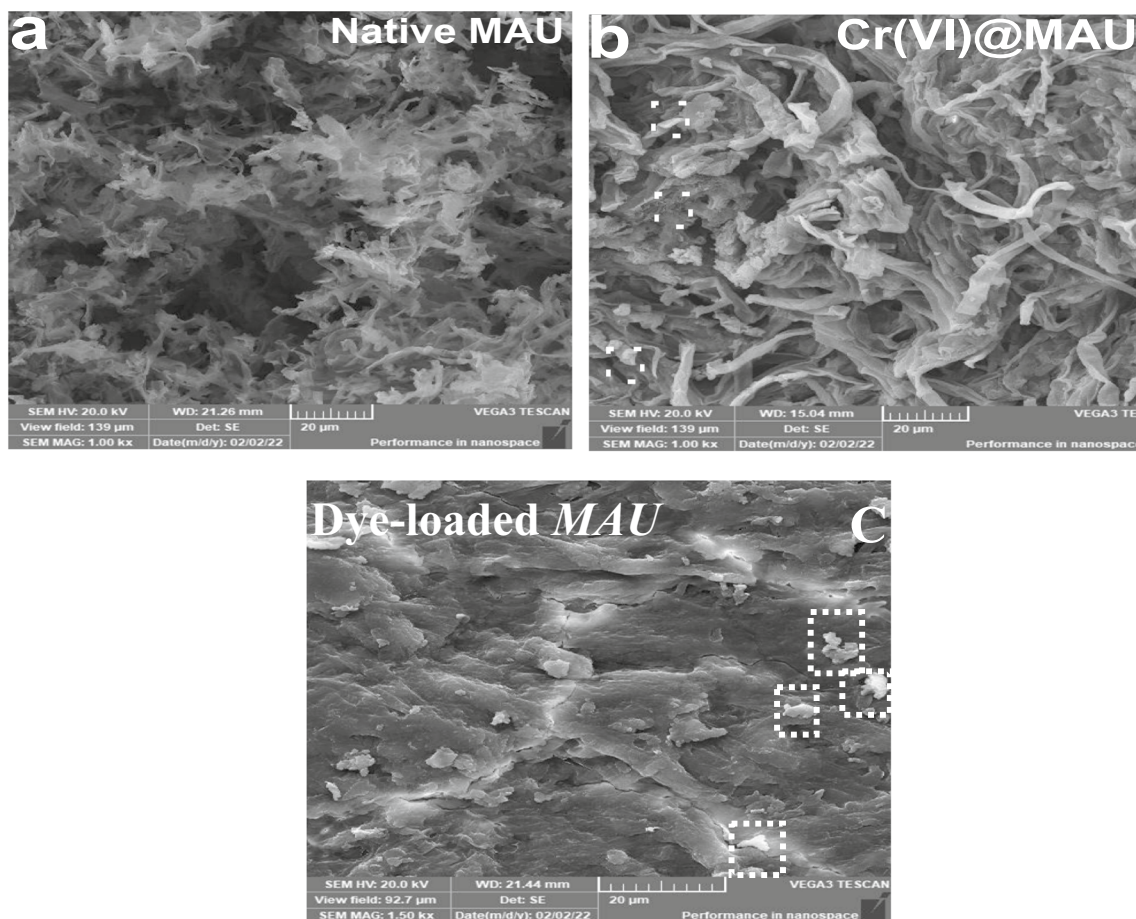
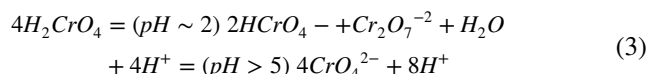


**Fig. 3** SEM spectra of (a) native MAU (b) Cr(VI)@MAU (c) dye-loaded MAU

adsorbents with surface charges. Figures 6(a-b) show the effect of the pH adsorbate solution on the adsorption capacity of MAU. Notably, improved adsorption was observed with a slight reduction in the acidity of the adsorbate solution, from pH 3.0 to 5.0 (for Cr(VI)@MAU) and from pH 2.0 to 3.0 (for dye-loaded MAU). Regarding the Cr(VI)@MAU (Fig. 6a), at pH 3.0, the surface of MAU is quite cationic due to the protonation of the partial amino groups ( $-\text{NH}_2$  converts to  $-\text{NH}_3^+$ ) within its chemical structure [43]. Also, the conversion of chromium ions into chromic acid ( $\text{H}_2\text{CrO}_4$ , Eq. 3) could prohibit the affinity between the Cr ions and the protonated site on the MAU. Upon the progressive reduction of the solution acidity, the adsorption capacity was increased due to improved electrostatic adsorption between chromium oxyanions ( $\text{HCrO}_4^-$  or  $\text{Cr}_2\text{O}_7^{2-}$ ) and positively charged groups of MAU like the amino and acetamide groups. Meanwhile, by increasing the pH beyond pH 5.0, the conversion of dichromate to monochromate ions (Eq. 3) is initiated, thus an adsorption capacity reduction [44].



For the dye-loaded MAU (Fig. 6b), at pH 2.0–3.0, there is a sufficient electrostatic attraction between the anionic AO142 species and the MAU surface groups, hence the observed increasing adsorption capacity. A further decrease in solution acidity resulted in electrostatic repulsion due to the presence of abundant  $\text{OH}^-$  ions on the MAU surface. Thus, the optimum pH

**Table 3** Elemental compositions of the raw and loaded adsorbents

Elements	Raw MAU	Cr(VI)@MAU	Dye-loaded MAU
C (wt %)	73.38	56.19	62.62
O (wt %)	26.62	41.53	24.79
S (wt %)	-	-	4.27
Cr (wt %)	-	0.78	-
N (wt %)	-	-	8.23
K (wt %)	-	1.50	0.09

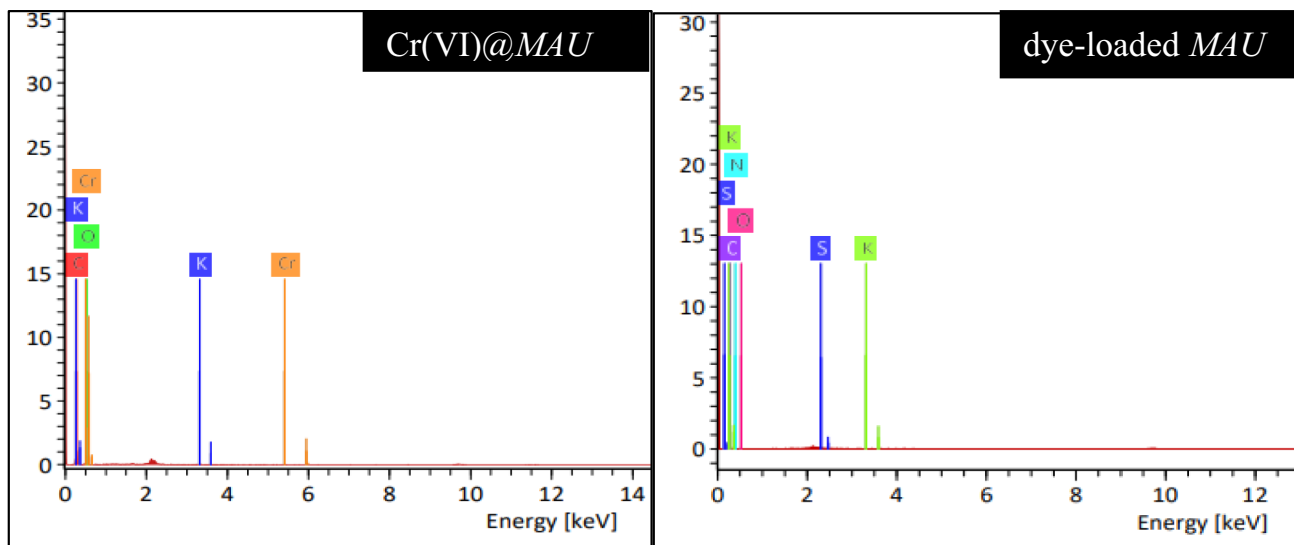


Fig. 4 EDX spectra of Cr(VI)@MAU and dye-loaded MAU

for Cr(VI) and AO142 adsorption was established at pH 5.0 and 3.0, respectively. The result further reveals that the impact of the electrostatic interaction mechanism is strongly evident in both adsorption systems.

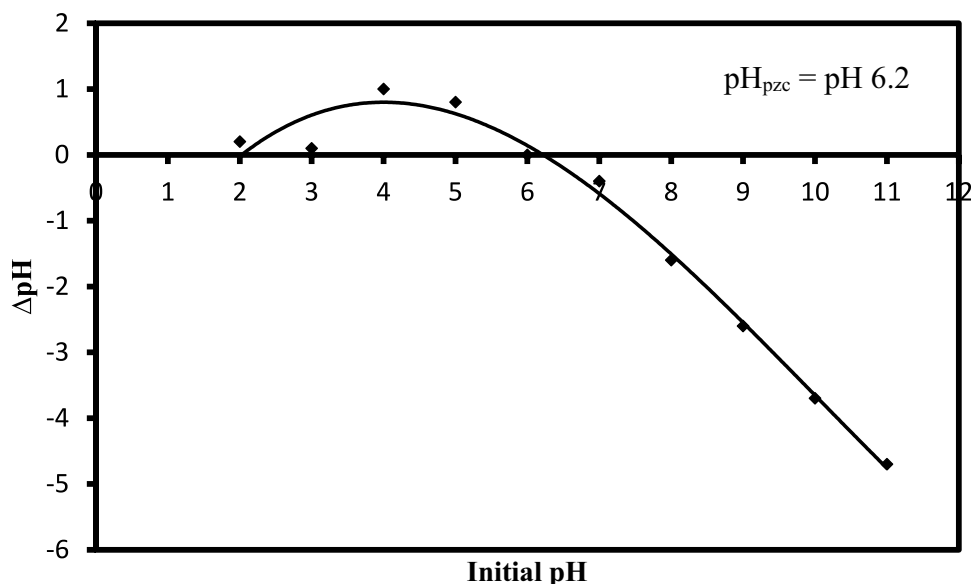
Table 4 Surface area and pore properties of MAU

Parameters	BET	BJH
Surface area (m <sup>2</sup> /g)	254.376	99.295
Pore volume (cm <sup>3</sup> /g)	-	0.178
Pore size (nm)	1.654	1.925

Effect of Adsorbent Concentration

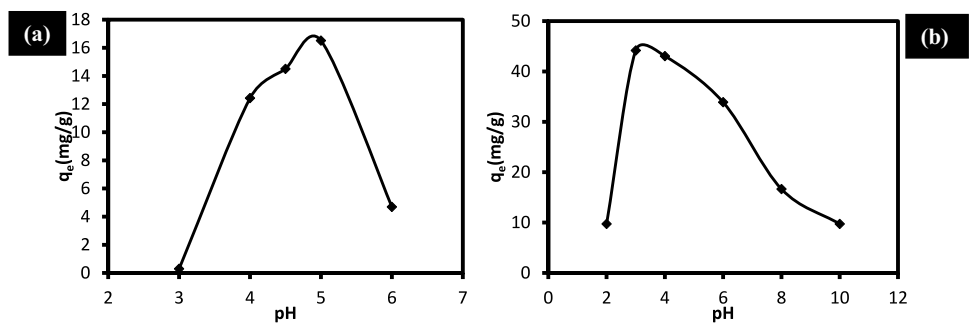
The relationship between the dose of adsorbent (g/L) and the adsorption capacity (q<sub>e</sub>, mg/g), as presented in Figs. 7(a-b) depicts a decreased adsorption capacity with increasing adsorbent dose. For instance, at 2.0 g/L dosage, the number of MAU active sites increases significantly, thus leading to their progressive unsaturation at constant adsorbate concentrations. Also, the probable agglomeration and clogging of MAU particles at high dosages further decrease the biosorbent surface area [45] and alter the adsorbate concentration flux [46]. Similarly, observation was have been reported previously in the literature [24, 47, 48].

Fig. 5 Plot for the determination of the MAU point of zero charge





**Fig. 6** Effect of pH on the adsorption of (a) Cr(VI) and (b) AO142 onto MAU. [Reaction conditions: 50 mg/L initial conc; 0.2 g/L adsorbent conc; contact time of 2 h; T, 30 °C]



**Effect of Contact Time**

Figures 8(a-b) show the relationship between adsorption time and adsorption capacity at specified operating conditions. At the onset of adsorption, a rapid increase in the adsorption capacities, which is due to the presence of enough vacant adsorption sites,

was observed. Also, the initial rapid uptake was possible due to the phenomenon of shortened diffusion path which ensured unrestricted adsorbate access to the nanofibrils morphology of the MAU [12]. Consequently, an equilibrium time of 80 and 120 min was achieved during the adsorption of Cr(VI) and AO142 dye, respectively. In conclusion, it was generally

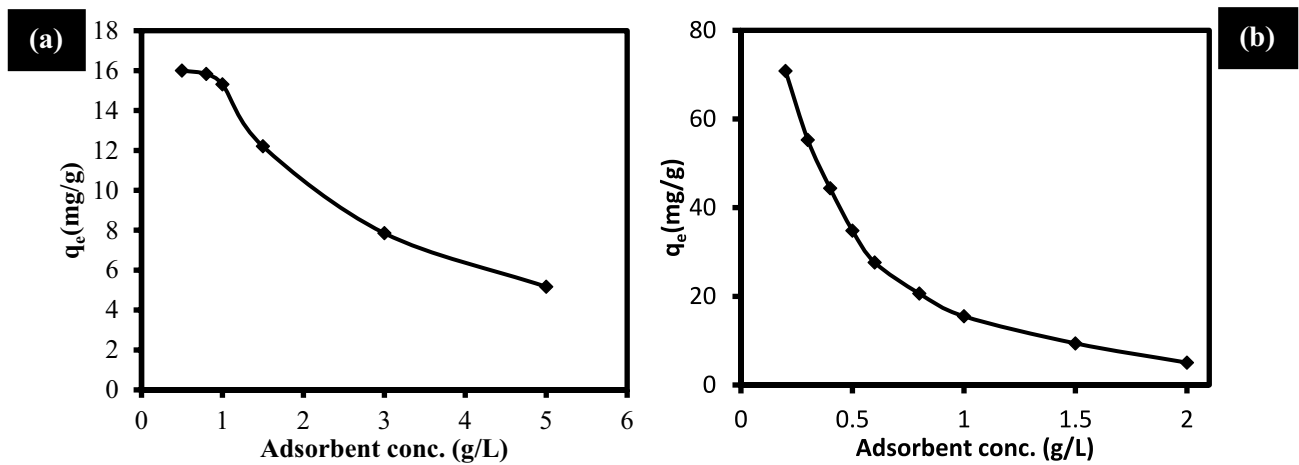


**Fig. 7** Effect of adsorbent concentration on the adsorption of (a) Cr(VI) and (b) AO142 [Reaction conditions: (a) 50 mg/L initial conc; 0.2 g/L adsorbent conc; contact time of 2 h; T, 30 °C; pH 5.0 (for Cr(VI)) and pH 3.0 (for AO142) adsorption]

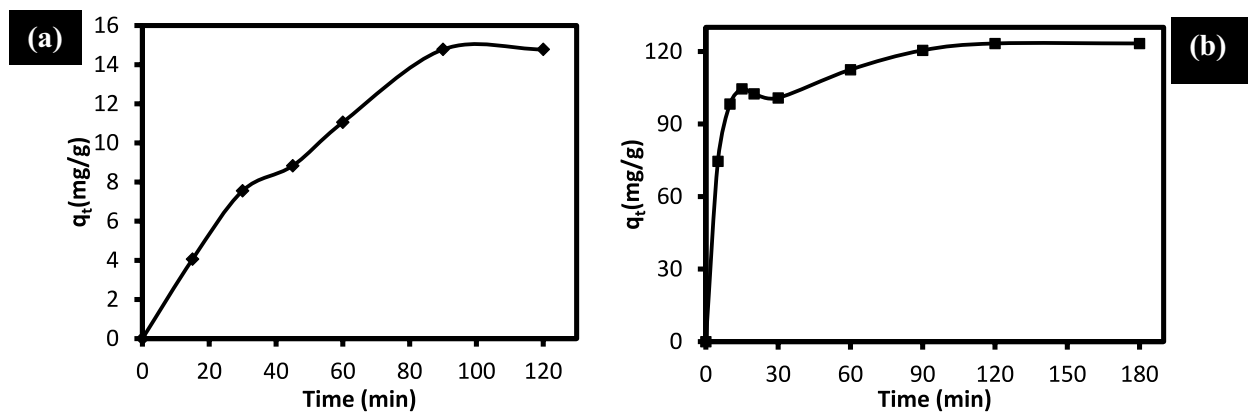


**Fig. 8** Effect of contact time on the adsorption of (a) Cr(VI) and (b) AO142. [Reaction conditions: (a) 50 mg/L initial conc; 0.2 g/L adsorbent conc; T, 30 °C and pH 5.0 (for Cr(VI)) and pH 3.0 (for AO142) adsorption]

**Table 5** Kinetics model parameters

PFO	PSO	Bangham
<b>Cr(VI)@MAU</b>		
$q_{e, cal} = 22.36$	$q_{e, cal} = 16.51$	$q_{e, cal} = 16.81$
$k_1 = 1.12$	$k_2 = 0.0007$	$k_b = 0.02$
<b>SNE = 2.43</b>	<b>SNE = 2.32</b>	$n = 0.98$
		<b>SNE = 2.50</b>
<b>Dye-loaded MAU</b>		
$q_{e, cal} = 17.11$	$q_{e, cal} = 18.15$	$q_{e, cal} = 18.71$
$k_1 = 0.20$	$k_2 = 0.0023$	$k_b = 0.41$
<b>SNE = 1.17</b>	<b>SNE = 1.13</b>	$n = 0.98$
		<b>SNE = 1.18</b>

The bold values provided the basis for selecting the model of best fit. Thus, the small the SNE value, the better the model fit

$q_{e, exp} = 15.24$  mg/g [for Cr(VI)@MAU] and 18.33 mg/g [for Dye-loaded MAU]

observed that the MAU exhibited better adsorption capacity for AO142 molecules than for Cr(VI) at the same optimal process condition. Although the reason behind the observation is not clear, however, the nature of the adsorbates played a vital role.

## Adsorption Modelling

### Kinetics Studies

Kinetic investigations are very important in any adsorption process for eventual scale-up studies. The kinetics study for Cr(VI) adsorption was investigated under the following reaction conditions: Cr(VI) conc., 10 mg/L; adsorbent conc., 0.2 g/L; pH 5.0; temperature, 30 °C. That of AO142 dye adsorption was investigated at 10 mg/L conc; 0.2 g/L adsorbent conc; pH 3.0; temperature, 30°. Consequently, the process kinetics was investigated using three classical kinetic

models whose theoretical background and mathematical expressions are presented in Section "Mathematical and theoretical backgrounds of the studied models" and Table 1. The generated model parameters and the respective nonlinear plots are presented in Table 5 and Fig. 9, respectively. Taking the SNE value (refer to Section "Error analysis") as the basis, the lower the value, the better the model description. Hence, the PSO model is considered the best fit for Cr(VI) and AO142 dye adsorption. The good fitting of the PSO model signifies the possibility of chemical interaction and complexation between the Cr (VI) ions and the functional groups of the MAU. Furthermore, the  $q_{e, cal}$ -value of the respective best-fit models exhibited a close correlation to the  $q_{e, exp}$ -value. Also, the  $k_2$ -value recorded in Table 5 was relatively much lower than the  $k_1$ -value for both adsorbates and thus, implies faster second-order rate sorption.

### Isotherm Studies

Isotherm studies quantify the relationship between the concentration of solute/adsorbate adsorbed onto the adsorbent ( $q_e$ , mg/g) and those still retained within the bulk fluid ( $C_e$ , mg/L) at equilibrium and constant temperature. The observation of an initial steep rising curvature in Fig. 10 (biosorption isotherm curve) shows the occurrence a typical of type I (L-type) isotherm [29] for both adsorbates.

The study further applied isotherm models for the effective description of the adsorption equilibrium. Notably, respective isotherm model parameters provide some guidance on the nature of the sorption interaction and surface properties of the adsorbent. The results from the isotherm studies are presented in Table 6 and Fig. 11. Based on the magnitude of the SNE value, the Temkin model is considered the best fit for both adsorbates and suggests a chemisorption process. This conclusion is in line with those made from the kinetics studies. Regarding

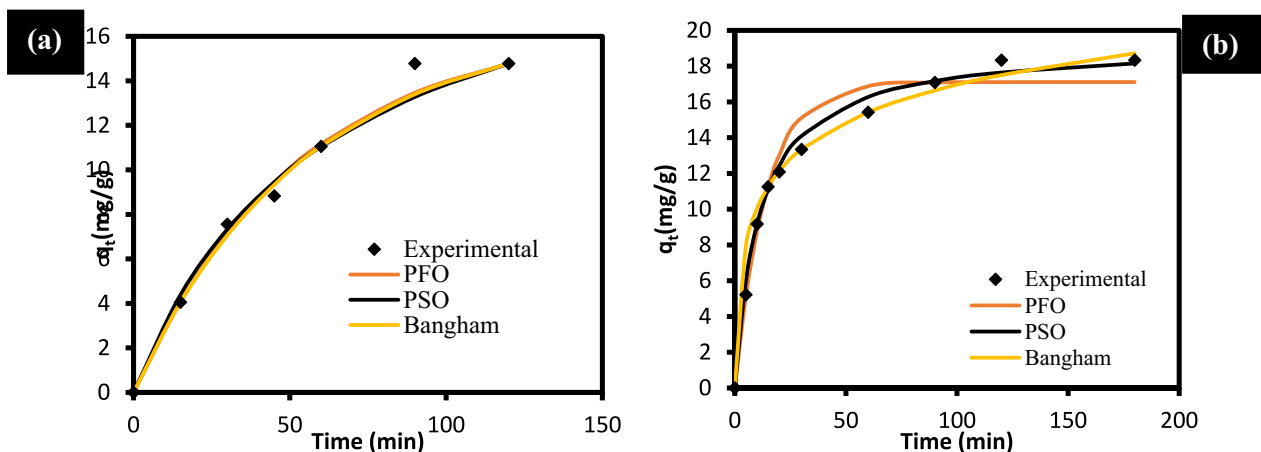


**Fig. 9** The kinetics plots for (a) Cr(VI) and (b) AO142 adsorption

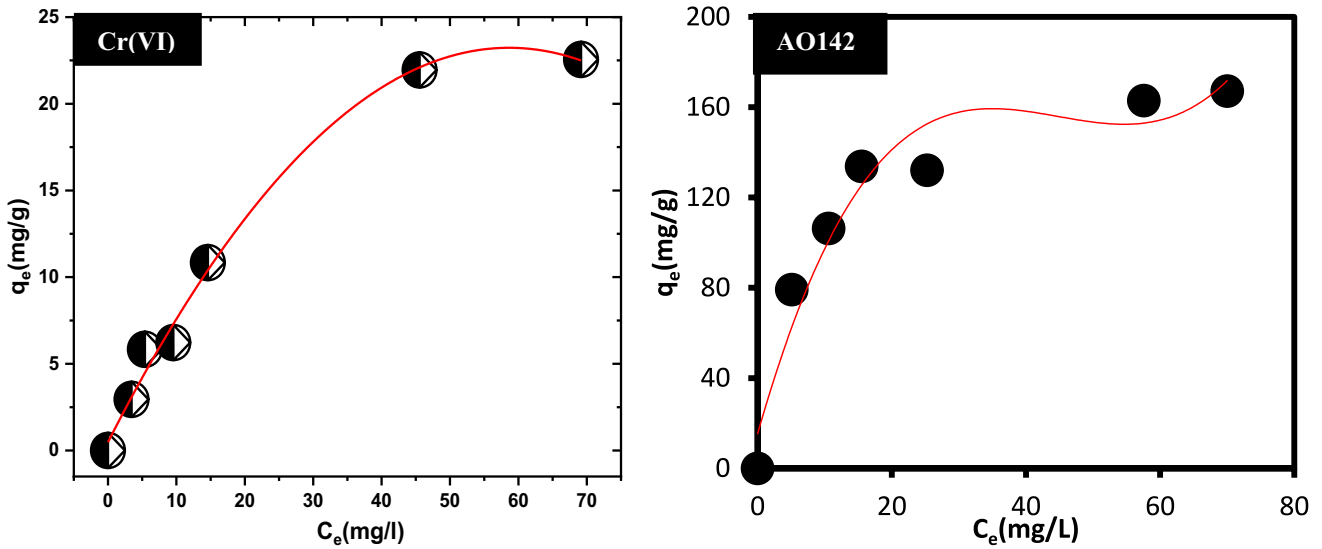


Fig. 10 Equilibrium adsorption isotherm for Cr(VI) and AO142 adsorption

Table 6 Isotherm model parameters

	Langmuir	Temkin	Freundlich	Hill	Sips	Toth
<b>Cr(IV) uptake</b>						
$q_{max}$ = 31.84	$A_T$ = 2.67	$n_F$ = 1.95	$q_{SH}$ = 200	$K_S$ = 3.14	$k_T$ = 2.40	
$K_L$ = 1.12	$b_T$ = 829.76	$K_F$ = 2.57	$n_H$ = 0.46	$\alpha_S$ = -0.05	$\alpha_T$ = 0.09	
$R_L$ = 0.035	<b>SNE = 1.611</b>	<b>SNE = 1.661</b>	$k_H$ = 618.66	$\beta_S$ = 0.40	$t$ = 2.13	
<b>SNE = 1.658</b>			<b>SNE = 1.85</b>	<b>SNE = 1.76</b>	<b>SNE = 1.62</b>	
<b>AO142 uptake</b>						
$q_{max}$ = 181.52	$A_T$ = 15.28	$n_F$ = 3.99	$q_{SH}$ = 201	$K_S$ = 5.87	$k_T$ = 5.96	
$K_L$ = 1.70	$b_T$ = 113.59	$K_F$ = 8.83	$n_H$ = 0.26	$\alpha_S$ = 0.0001	$\alpha_T$ = 0.009	
$R_L$ = 0.15	<b>SNE = 1.100</b>	<b>SNE = 1.109</b>	$k_H$ = 33.39	$\beta_S$ = 0.25	$t$ = 1.33	
<b>SNE = 1.148</b>			<b>SNE = 1.105</b>	<b>SNE = 1.109</b>	<b>SNE = 1.109</b>	

The bold values provided the basis for selecting the model of best fit. Thus, the small the SNE value, the better the model fit

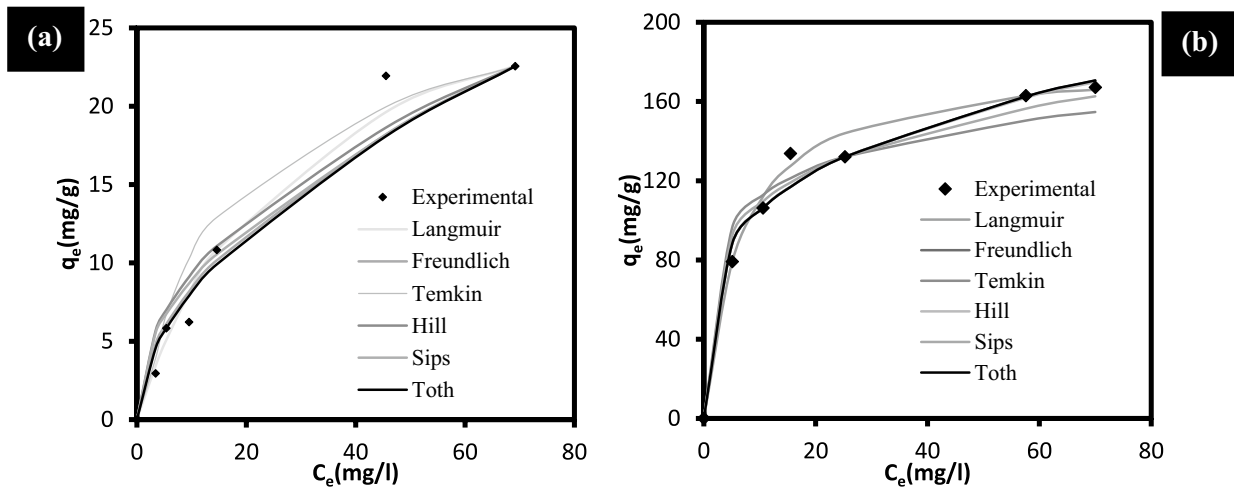


Fig. 11 The Isotherm model plots for (a) Cr(VI) and (b) AO142 adsorption

the other model parameters, the implication to the present system is summarily presented herein. The  $K_L$  value of 1.12 and 1.70 L/g for Cr(VI) and AO142 uptake, respectively suggest that the adsorbent exhibit reasonable affinity for the adsorbate [49, 50]. Also, the  $R_L$  value of 0.035 and 0.15 for Cr(VI) and AO142 uptake is indicative of a favourable adsorption process [51, 52]. The positive heat of adsorption ( $b_T$ ) parameter recorded for the Temkin model for both adsorbates is far greater than unity and thus an endothermic process is favoured. Based on the literature, the Sip model respectively reduces to Freundlich and Langmuir model at  $\beta_S$ -value equal to 1 and 0 [53]. The  $\beta_S$  value of 0.40 and 0.25 for Cr(VI) and AO142 uptake suggests that both systems are tending to Freundlich characteristics. The cooperative adsorption index for the Hill model ( $n_H$ ) was less than unity and indicates negative cooperativity, hence, the MAU affinity for other ligands is progressively limited as the adsorption duration extends [54, 55]. The “t” parameter of the Toth model provides insight into the heterogeneity of the adsorption system. Thus, a given adsorption system is considered heterogenous at  $t > 1$  [56]. On this basis, the present system is a heterogenous one and this conclusion corroborates the parametric indication from the Sip model.

## Probable Adsorption Mechanism

The involvement of some specific functional groups and donor sites for pollutant adsorption was verified via dedicated instrumental characterization of the adsorbent. Considering the XRD spectra, no significant structural changes were recorded as the major peaks were retained. Only a relative increase in the intensity of these peaks was observed and this indicates the occurrence of a physical adsorption process. From the FTIR spectra, the peak of the primary and secondary amines located between 1660 to 1500  $\text{cm}^{-1}$  generally diminished due to the deprotonation of the Lewis basicity of  $-\text{NH}$  and  $-\text{NH}_2$  by the Lewis acidic nature of Cr (VI) and N-heterocyclic nitrogen of the AO142 dye. This suggests a coordinate bonding between respective adsorbates and nitrogen-containing groups on the MAU. Furthermore, the nitrogen and oxygen functional groups were also responsible for  $n-\pi$  (electron-acceptor) interaction, another probable sorption mechanism in this study. The  $n-\pi$  (electron-acceptor) interaction mechanism is evidenced in the post-adsorption variation in the peak intensity and wavenumber shift observed in the C–O–C and C–O stretching groups. Also, the nitrogen/oxygen-containing groups play a prominent role during the binding of both adsorbates. Notably,

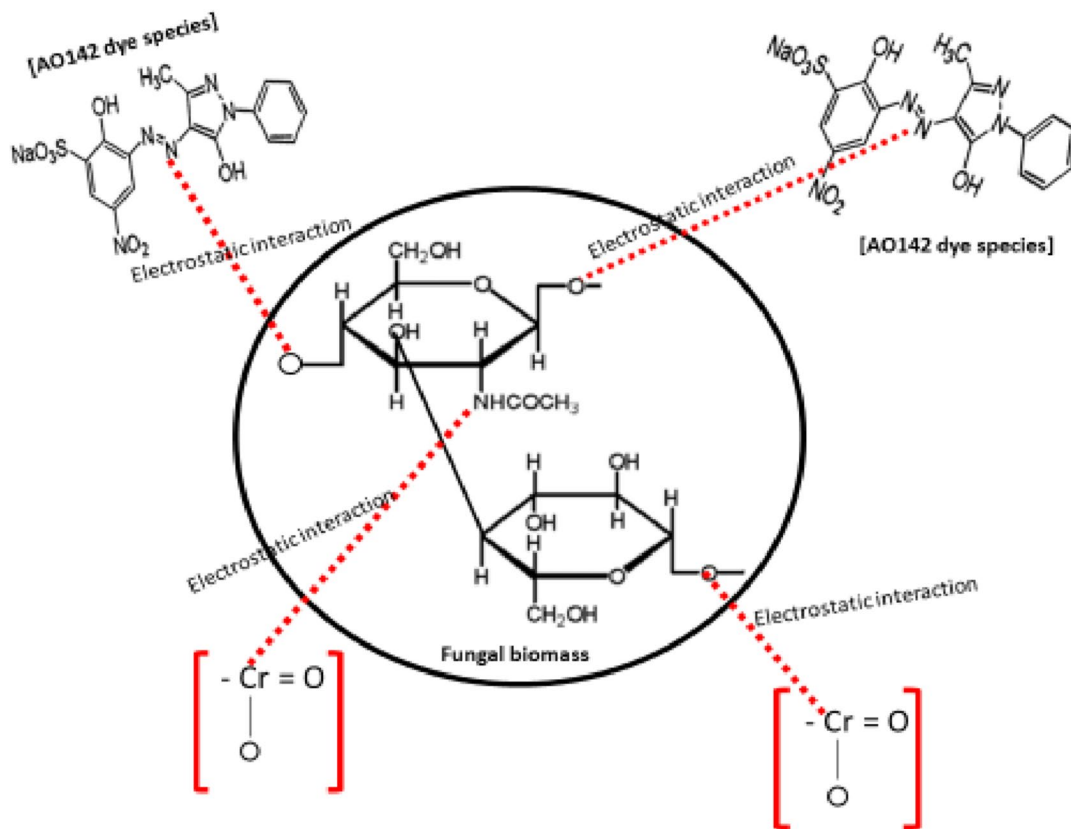


Fig. 12 Illustration of the electrostatic interaction mechanism

**Table 7** Estimated cost of producing 1 kg of MAU

S/N	Material	Number of units	Net price (USD)
1	Potato Dextrose Broth (PDB)	9.60 kg	30.72
2	Energy cost for drying (80 °C, 2 h)	1.00 kWh	0.83
	Net price	-	<b>31.55</b>
5	Other overhead costs (5% of the net cost)	-	1.58
	<b>Total cost</b> <b>[net + overhead cost]</b>		<b>33.13</b>

The bold values provided the basis for selecting the model of best fit. Thus, the smaller the SNE value, the better the model fit

the charged adsorbate species bind to the nitrogen-/oxygen-based groups on the MAU via an electrostatic interaction mechanism as shown in Fig. 12.

### Cost Analysis for Adsorbent Production

Adsorbent production costing is necessary for determining the economic feasibility and sustainability of an adsorption system. It is also necessary for scale-up studies. Superficially, the adsorbent production cost can be presented as an arithmetic sum of the raw material, reagent and energy costs as shown in Table 7. According to the Table, the cost of producing 1 kg of MAU is about USD 33.13. Furthermore, in terms of adsorption process efficiency, Ighalo et al. [57] noted that adsorbent cost analysis can be considered either in terms of the adsorbent cost per gram of the adsorbate removed. Consequently, the lower the adsorption cost, the better the operational and economic feasibility of the system. The substitution of the experimental adsorption capacity (see Table 5) and the cost per kg of adsorbent (see Table 7) into Eq. (4) gives the adsorption cost of 2.17 and 1.81 USD per mg/g for Cr(VI) and AO142 dye species, respectively. Thus, the use of MAU for treating AO142 dye-contaminated wastewater is economically more feasible and sustainable compared to that of Cr(VI) contaminated wastewater.

$$\text{Adsorption cost} = \frac{\text{Cost per kg of adsorbent (EGP)}}{\text{Adsorption capacity of adsorbent } \left(\frac{\text{mg}}{\text{g}}\right)} \quad (4)$$

### Environmental Implications

Following every successful adsorption cycle, the adsorbent gets solely saturated such that its adsorption capacity is completely lost with time. However, based on the principles of green Engineering, such exhausted adsorbent should be regenerated and reused. To ensure an efficient adsorbent regeneration, the choice of eluents is paramount and to make an informed choice of eluent, the nature of the adsorbent and the predominant sorption mechanism should be considered. In addition to being effective,

a choice eluent should also be cheaply available, non-destructive to the adsorbent and ecofriendly [58].

The Cr(VI) adsorbed to the MAU biomass can be readily regenerated using cheaply available and eco-friendly dilute minerals and organic acids [59]. Using dilute sodium hydroxide and hydrochloric acid solutions, O'mahony et al. [60] demonstrated successful desorption of nickel, copper, zinc and cadmium cations from *Penicillium* biomass. However, the success of an alkaline and acid solution in desorbing heavy metal depends on the adsorbent surface charge and charge on the pollutant species [61, 62]. Furthermore, regarding the desorption of the anionic AO142 dye species, a dilute alkaline solution is used as an eluent. Consequent upon impregnation in a dilute alkaline solution (eluent), the MAU surface becomes deprotonated. Thus, the anionic AO142 dye species which were mostly bound electrostatically to the adsorbent surface would be readily dislodged via an electrostatic repulsion mechanism. This approach was successfully applied for the desorption of reactive yellow 2 dye from *Corynebacterium glutamicum* waste biomass [63].

After several adsorption–desorption cycles, the adsorption capacity of the adsorbent gets ultimately exhausted. However, handling these exhausted adsorbents and the solute-laden eluent solutions pose a challenge which must be cooperatively addressed to avoid creating more complex scenarios. To mitigate the aforementioned post-desorption challenges, the exhausted adsorbent can be safely disposed of using an appropriate approach, while the solute (especially heavy metals) can be recovered from the saturated eluent via either metal precipitation, or electrowinning [61, 64]. The Cr(VI) can also be transformed into a less toxic form via an oxidation–reduction reaction. Due to the minimal toxicity of the AO142 dye species used in this study, the spent MAU could be safely dumped in dedicated landfills after proper and effective desorption of the adsorbed dye [65]. The process of landfilling has the advantage of cost-effectiveness and flexibility.

### Adsorbent Performance Comparison

The adsorptive performance of a given adsorbent is often expressed as a function of the amount of solute adsorbed

**Table 8** Comparison of the adsorptive performance of different adsorbents in terms of the  $q_{\max}$  values

Adsorbent	Adsorbate	Process variable				$q_{\max}$ (mg/g)	Ref
		pH	Time (min)	Adsorbent dose (g/L)	Initial conc		
Mixed <i>A. niger</i> and <i>A. flavus</i>	Reactive green 6 dye	5.0	50.0	2.5	25	21.20	[67]
Mixed <i>A. niger</i> and <i>A. flavus</i>	Cu <sup>2+</sup>	5.0	50.0	2.5	25	24.92	[67]
<i>Aspergillus Ustus</i>	Cr(VI)	5.0	80.0	0.5	50	31.84	<b>Present Study</b>
<i>Aspergillus campestris</i>	Cu <sup>2+</sup>	6.0	30.0	1.0	50	62.02	[68]
<i>Penicillium sp.</i>	Ni <sup>2+</sup>	5.5	140.0	7.5	639	63.60	[69]
<i>Trichoderma harzianum</i>	Reactive Red-3 dye	4.0	150.0	0.5	100	172.63	[70]
<i>Aspergillus Ustus</i>	Acid Orange 142 dye	3.0	120.0	0.2	50	181.52	<b>Present study</b>
Mixed <i>A. fumigatus</i> and <i>A. niger</i>	Cr(VI)	2.0	60.0	0.7	500	249.90	[71]

The bold values provided the basis for selecting the model of best fit. Thus, the small the SNE value, the better the model fit

per unit mass of the adsorbent. Igwegbe et al. [66] reported that the rating of adsorption performance based on the % removal efficiency does not accurately reflect how well the adsorbent performs since it is heavily reliant on the initial adsorbate concentration and adsorbent dosage. Conversely, the adsorption capacity (mg/g) shows the inherent adsorption capacity of the different adsorbents. Table 8 presents the adsorption performance of different fungal-based adsorbents for adsorbing selected heavy metals and dye molecules, in ascending order of their respective  $q_{\max}$  (mg/g). Due to the surface charge of the fungal biomass, it was observed that the optimum uptake occurred within the acidic pH ranges, irrespective of the adsorbate type. Consequently, the adsorption capacities reported in the present study are well within existing values obtainable in the literature.

## Conclusion

In this research, the mycelium of *Aspergillus ustus* (MAU) was successfully isolated and further applied as an efficient adsorbent for the adsorption of Cr (VI) ions and acid orange 142 (AO142) dye. The pre and post-adsorption characteristics of the MAU were evaluated by FTIR, XRD, SEM, and EDX analyses. The presence of the functional groups relevant for adsorbing the respective pollutants was confirmed from the FTIR analysis. Similarly, the XRD and SEM analyses elucidated the structural and morphological properties of the MAU, while the EDX analysis confirms the Cr and AO142 dye adsorption. At optimum process conditions, it was generally observed that the MAU exhibited better adsorption capacity for AO142 molecules than for Cr(VI) at the same conditions. Although the reason behind the observation is not clear, however, the nature of the adsorbates played a vital role.

**Authors' Contributions** • L.A. Mohamed: Experimentation, Formal analyses, Data curation.

• Chukwunonso O. Aniagor: Conceptualization, Data curation, Supervision, Writing – Original draft, Writing – Review and editing.

• A.A. Aly: Experimentation, Formal analyses, Data curation.

• A. Hashem: Project administration, Data curation, Supervision, Writing – Review and editing.

**Funding** There was no external funding for the study.

**Data Availability** All data generated or analyzed during this study are included in this published article.

## Declarations

**Competing Interests** The authors declare no competing interests.

**Ethical Approval** Not applicable.

**Conflict of Interest** The authors declare that there are no conflicts of interest and there exist *no relationships or activities that could appear to have influenced the submitted work.*

## References

- Onuzulike CM, Aniagor CO, Modekwe GO, Ejimofor MI, Menkiti MC (2022) Remediation of Lead Ion Contaminated Stream Using Biosurfactant-Functionalized Mesoporous Activated Carbon. *Chemistry Africa*. <https://doi.org/10.1007/s42250-022-00316-5>
- Babarinde A, Babalola JO, Adegoke J, Osundeko AO, Olasehinde S, Omodehin A, Nurhe E (2013) Biosorption of Ni (II), Cr (III), and Co (II) from solutions using *Acalypha hispida* leaf: kinetics, equilibrium, and thermodynamics. *J Chem*. Article ID 460635. <https://doi.org/10.1155/2013/460635>
- Jing X, Cao Y, Zhang X, Wang D, Wu X, Xu H (2011) Biosorption of Cr (VI) from simulated wastewater using a cationic surfactant modified spent mushroom. *Desalination* 269(1–3):120–127
- Saha B, Orvig C (2010) Biosorbents for hexavalent chromium elimination from industrial and municipal effluents. *Coord Chem Rev* 254(23–24):2959–2972

5. Asfaw TB, Tadesse TM, Ewnetie AM (2017) Determination of total chromium and chromium species in Kombolcha tannery wastewater, surrounding soil, and lettuce plant samples, South Wollo. Ethiopia Adv Chem 2017:1–7
6. Mohamed LA, Aniagor CO, Hashem A (2021) Isotherms and kinetic modelling of mycoremediation of hexavalent chromium contaminated wastewater. Clean Eng Technol 4:100192
7. Menkiti MC, Aniagor CO, Onuzulike CM, Ejimofor MI, Okonkwo SS (2022) Chromium adsorption from petroleum refinery wastewater using biocomposites. Results Surf Interfaces 8:100064. <https://doi.org/10.1016/j.rsufi.2022.100064>
8. Kalsoom A, Batool R (2020) Biological and Nonbiological Approaches for Treatment of Cr (VI) in Tannery Effluent. Emerging Eco-friendly Green Technologies for Wastewater Treatment. Springer, pp 147–170
9. Sankhla MS, Kumar R, Prasad L (2019) Distribution and contamination assessment of potentially harmful element chromium in water. International Medico-Legal Reporter Journal, 2 (3). <https://doi.org/10.2139/ssrn.3492307>
10. Jeřábková J, Tejnecký V, Borůvka L, Drábek O (2018) Chromium in anthropogenically polluted and naturally enriched soils: a review. Sci Agric Bohem 49(4):297–312
11. Kumar A, Dixit U, Singh K, Gupta SP, Beg MSJ (2021) Structure and properties of dyes and pigments, in dyes and pigments-novel applications and waste treatment. IntechOpen. <https://doi.org/10.5772/intechopen.97104>
12. Hashem A, Aniagor CO, Farag S, Abou-Okeil AA, Aly AA, Amr A (2022) Lepidium sativum Seed Powder: A Novel Biosorbent for Acid Orange 142 Dye Uptake. Environ Process 9(4):1–20
13. Lellis B, Fávaro-Polonio CZ, Pamphile JA, Polonio JC (2019) Effects of textile dyes on health and the environment and bioremediation potential of living organisms. Biotechnol Res Innov 3(2):275–290
14. Rangabhashiyam S, Anu N, Nandagopal MG, Selvaraju N (2014) Relevance of isotherm models in biosorption of pollutants by agricultural byproducts. J Environ Chem Eng 2(1):398–414
15. Baral A, Engelken RD (2002) Chromium-based regulations and greening in metal finishing industries in the USA. Environ Sci Policy 5(2):121–133
16. Hashem A, Aniagor CO, Abdel-Halim E, Amr A, Farag S, Aly A (2022) Instrumental characteristics and acid blue 193 dye sorption properties of novel lupine seed powder. Clean Chem Eng 2:100011. <https://doi.org/10.1016/j.clce.2022.100011>
17. Hashem A, Aniagor C, Hussein D, Farag S (2021) Application of novel butane-1, 4-dioic acid-functionalized cellulosic biosorbent for aqueous cobalt ion sequestration. Cellulose 28(6):3599–3615
18. Hashem A, Aniagor C, Taha GM, Fikry M (2021) Utilization of low-cost sugarcane waste for the adsorption of aqueous Pb (II): kinetics and isotherm studies. Curr Res Green Sustain Chem 4:100056
19. Kabbout R, Taha S (2014) Biodecolorization of textile dye effluent by biosorption on fungal biomass materials. Phys Procedia 55:437–444
20. Sharma KR, Naruka A, Raja M, Sharma RK (2022) White rot fungus mediated removal of mercury from wastewater. Water Environ Res 94(7):e10769
21. Mo J, Liu Y, Gao X, Zhou S, Deng Y, Ke Y, Peng L, Li H, Chen S, Long J (2022) Potential application of Fusarium fungal strains (Fusarium sp. FP, Arthrinium sp. FB, and Phoma sp. FR) for removal of Tl (I) ions from water. Environ Sci Pollut Res 29:46049–46063. <https://doi.org/10.1007/s11356-022-18791-1>
22. Mohamed LA, Aniagor CO, Taha GM, Abou-Okeil A, Hashem A (2021) Mechanistic investigation of the mass transfer stages involved during the adsorption of aqueous lead onto Scopulariopsis brevicompectum fungal biomass. Environ Challenges 5:100373
23. Almeida E, Corso C (2019) Decolorization and removal of toxicity of textile azo dyes using fungal biomass pelletized. Int J Environ Sci Technol 16(3):1319–1328
24. Hashem A, Aniagor CO, Morsy OM, Abou-Okeil A, Aly A (2022) Apricot seed shell: an agro-waste biosorbent for acid blue193 dye adsorption. Biomass Convers Biorefinery. <https://doi.org/10.1007/s13399-022-03272-9>
25. Wiryawan A, Retnowati R, Burhan P, Syekhiani S (2018) Method of analysis for determination of the chromium (Cr) species in water samples by spectrophotometry with diphenylcarbazide. J Environ Eng Sustain Technol 5(1):37–46
26. Ho Y-S, McKay G (1999) Pseudo-second order model for sorption processes. Process Biochem 34(5):451–465
27. Aniagor C, Menkiti M (2018) Kinetics and mechanistic description of adsorptive uptake of crystal violet dye by lignified elephant grass complexed isolate. J Environ Chem Eng 6(2):2105–2118
28. Leaist DG, Hao L (1994) Simultaneous measurement of mutual diffusion and intradiffusion by Taylor dispersion. J Phys Chem 98(17):4702–4706
29. Al-Ghouti MA, Da'ana DA (2020) Guidelines for the use and interpretation of adsorption isotherm models: A review. J Hazard. Mater 93:122383. <https://doi.org/10.1016/j.jhazmat.2020.122383>
30. Menkiti M, Aniagor C (2018) Parametric studies on descriptive isotherms for the uptake of crystal violet dye from aqueous solution onto lignin-rich adsorbent. Arab J Sci Eng 43(5):2375–2392
31. Ho Y, Porter J, McKay G (2002) Equilibrium isotherm studies for the sorption of divalent metal ions onto peat: copper, nickel and lead single component systems. Water Air Soil Pollut 141(1–4):1–33
32. Aniagor CO, Abdel-Halim ES, Hashem A (2021) Evaluation of the aqueous Fe (II) ion sorption capacity of functionalized microcrystalline cellulose. J Environ Chem Eng 9(4):105703
33. Hashem A, Aniagor CO, Nasr MF, Abou-Okeil A (2021) Efficacy of treated sodium alginate and activated carbon fibre for Pb (II) adsorption. Int J Biol Macromol 176:201–216
34. Cristiano E, Hu Y-J, Siegfried M, Kaplan D, Nitsche H (2011) A comparison of point of zero charge measurement methodology. Clays Clay Miner 59(2):107–115
35. Abdel-Mohsen AM, Frankova J, Abdel-Rahman RM, Salem AA, Sahffie NM, Kubena I, Jancar J (2020) Chitosan-glucon complex hollow fibers reinforced collagen wound dressing embedded with aloe vera. II. Multifunctional properties to promote cutaneous wound healing. Int J Pharm 582:119349
36. Abdel-Mohsen AM, Jancar J, Massoud D, Fohlerova Z, Elhadidy H, Spatz Z, Hebeish A (2016) Novel chitin/chitosan-glucon wound dressing: Isolation, characterization, antibacterial activity and wound healing properties. Int J Pharm 510(1):86–99
37. Beran K, Holan Z, Baldrían J (1972) The chitin-glucon complex in Saccharomyces cerevisiae. I. IR and x-ray observations. Folia Microbiol (Praha) 17(5):322–330
38. Abdel-Rahman RM, Vishakha V, Kelnar I, Jancar J, Abdel-Mohsen AM (2022) Synergistic performance of collagen-g-chitosan-glucon fiber biohybrid scaffold with tunable properties. Int J Biol Macromol 202:671–680
39. Zhou J, Liu LL, Cao LL, Stephan DW (2018) Nitrogen-Based Lewis Acids: Synthesis and Reactivity of a Cyclic (Alkyl)(Amino) Nitrenium Cation. Angew Chem Int Ed 57(13):3322–3326
40. Brunauer S, Emmett PH, Teller E (1938) Adsorption of gases in multimolecular layers. J Am Chem Soc 60(2):309–319
41. Zdravkov B, Čermák J, Šefara M, Janků J (2007) Pore classification in the characterization of porous materials: A perspective. Open Chem 5(2):385–395

42. Mays T (2007) A new classification of pore sizes. *Stud Surf Sci Catal* 160(Characterization of Porous Solids VII):57–62
43. Hashem A, Okeil A, Fikry M, Aly A, Aniagor C (2021) Isotherm and kinetics parametric studies for aqueous Hg (II) uptake onto N-[2-(methylamino) ethyl] ethane-1, 2-diaminated acrylic fibre. *Arab J Sci Eng* 46(7):6703–6714
44. Li Y, Shan S, Yang R, Gai X, Mao J, Huang N, Tou Y, Meas A (2016) Preparation of bamboo biochars by low-temperature hydrothermal method and its adsorption of organics. *Trans Chinese Soc Agric Eng* 32(24):240–247
45. Aniagor CO, Afifi M, Hashem A (2021) Modelling of basic blue-9 dye sorption onto hydrolyzed polyacrylonitrile grafted starch composite. *Carbohydrate Polymer Technol App* 2:100141
46. Ohale PE, Onu CE, Nwabanne JT, Aniagor CO, Okey-Onyesolu CF, Ohale NJ (2022) A comparative optimization and modeling of ammonia–nitrogen adsorption from abattoir wastewater using a novel iron-functionalized crab shell. *Appl Water Sci* 12(8):1–27
47. Aniagor CO, Afifi M, Hashem A (2021) Rapid and efficient uptake of aqueous lead pollutant using starch-based superabsorbent hydrogel. *Polym Bull.* <https://doi.org/10.1007/s00289-021-03817-4>
48. Aniagor CO, Taha GM, Badawy SM, El-Naggar ME, Hashem A (2022) Preparation of a novel acrylic fiber-based hydrogel and its utilization for the removal of aqueous lead ion. *J Market Res* 18:1450–1459
49. Alkurdi SS, Al-Juboori RA, Bundschuh J, Bowtell L, Marchuk A (2021) Inorganic arsenic species removal from water using bone char: A detailed study on adsorption kinetic and isotherm models using error functions analysis. *J Hazard Mater* 405:124112
50. Azizian S, Haerifar M, Basiri-Parsa J (2007) Extended geometric method: a simple approach to derive adsorption rate constants of Langmuir-Freundlich kinetics. *Chemosphere* 68(11):2040–2046
51. Chowdhury S, Saha P (2010) Sea shell powder as a new adsorbent to remove Basic Green 4 (Malachite Green) from aqueous solutions: Equilibrium, kinetic and thermodynamic studies. *Chem Eng J* 164(1):168–177
52. Igwegbe CA, Aniagor CO, Oba SN, Yap P-S, Iwuchukwu FU, Liu T, de Souza EC, Ighalo JO (2021) Environmental protection by the adsorptive elimination of acetaminophen from water: a comprehensive review. *J Ind Eng Chem* 104:117–135
53. Aniagor CO, Menkiti MC (2020) Relational description of an adsorption system based on isotherm, adsorption density, adsorption potential, hopping number and surface coverage. *Sigma J Eng Nat Sci* 38(3):1073–1098
54. Chen X, Hossain MF, Duan C, Lu J, Tsang YF, Islam MS, Zhou Y (2022) Isotherm models for adsorption of heavy metals from water-A review. *Chemosphere* 307:135545. <https://doi.org/10.1016/j.chemosphere.2022.135545>
55. Majd MM, Kordzadeh-Kermani V, Ghalandari V, Askari A, Sillanpää M (2021) Adsorption isotherm models: A comprehensive and systematic review (2010–2020). *Sci Total Environ* 812:151334. <https://doi.org/10.1016/j.scitotenv.2021.151334>
56. Podder M, Majumder C (2019) Bacteria immobilization on neem leaves/MnFe<sub>2</sub>O<sub>4</sub> composite surface for removal of As (III) and As (V) from wastewater. *Arab J Chem* 12(8):3263–3288
57. Ighalo JO, Omoarukhe FO, Ojukwu VE, Iwuozor KO, Igwegbe CA (2022) Cost of adsorbent preparation and usage in wastewater treatment: A review. *Clean Chem Eng* 3:100042. <https://doi.org/10.1016/j.clce.2022.100042>
58. Dhankhar R, Hooda A (2011) Fungal biosorption—an alternative to meet the challenges of heavy metal pollution in aqueous solutions. *Environ Technol* 32(5):467–491
59. Puranik P, Paknikar K (1997) Biosorption of lead and zinc from solutions using *Streptoverticillium cinnamomeum* waste biomass. *J Biotechnol* 55(2):113–124
60. O'mahony T, Guibal E, Tobin J (2002) Reactive dye biosorption by *Rhizopus arrhizus* biomass. *Enzyme Microbial Technol* 31(4):456–463
61. Baskar AV, Bolan N, Hoang SA, Sooriyakumar P, Kumar M, Singh L, Jasemizad T, Padhye LP, Singh G, Vinu A (2022) Recovery, regeneration and sustainable management of spent adsorbents from wastewater treatment streams: A review. *Sci Total Environ* 822:153555. <https://doi.org/10.1016/j.scitotenv.2022.153555>
62. Gupta S, Sireesha S, Sreedhar I, Patel CM, Anitha K (2020) Latest trends in heavy metal removal from wastewater by biochar based sorbents. *J Water Process Eng* 38:101561
63. Won SW, Yun Y-S (2008) Biosorptive removal of Reactive Yellow 2 using waste biomass from lysine fermentation process. *Dyes Pigm* 76(2):502–507
64. Prasad S, Yadav KK, Kumar S, Gupta N, Cabral-Pinto MM, Rezaania S, Radwan N, Alam J (2021) Chromium contamination and effect on environmental health and its remediation: A sustainable approaches. *J Environ Manage* 285:112174
65. Dhillon GS, Rosine GML, Kaur S, Hegde K, Brar SK, Drogui P, Verma M (2017) Novel biomaterials from citric acid fermentation as biosorbents for removal of metals from waste chromated copper arsenate wood leachates. *Int Biodeterior Biodegradation* 119:147–154
66. Igwegbe CA, Oba SN, Aniagor CO, Adeniyi AG, Ighalo JO (2021) Adsorption of ciprofloxacin from water: a comprehensive review. *J Ind Eng Chem* 93:57–77
67. Saravanan A, Karishma S, Kumar PS, Varjani S, Yaashikaa P, Jeevanantham S, Ramamurthy R, Reshma B (2021) Simultaneous removal of Cu (II) and reactive green 6 dye from wastewater using immobilized mixed fungal biomass and its recovery. *Chemosphere* 271:129519
68. Saravanan A, Sundararaman T, Jeevanantham S, Karishma S, Kumar PS, Yaashikaa P (2020) Effective adsorption of Cu (II) ions on sustainable adsorbent derived from mixed biomass (*Aspergillus campestris* and agro waste): optimization, isotherm and kinetics study. *Groundw Sustain Dev* 11:100460
69. Sundararaju S, Manjula A, Kumaravel V, Muneeswaran T, Vennila T (2020) Biosorption of nickel ions using fungal biomass *Penicillium* sp. MRF1 for the treatment of nickel electroplating industrial effluent. *Biomass Convers Biorefin* 12:1059–1068. <https://doi.org/10.1007/s13399-020-00679-0>
70. Karthik V, Kumar PS, Harsha Vardhan K, Saravanan K, Nithyakala N (2022) Adsorptive behaviour of surface tailored fungal biomass for the elimination of toxic dye from wastewater. *Int J Environ Anal Chem* 102(16):4710–4725
71. Saravanan A, Kumar PS, Govarthanan M, George CS, Vaishnavi S, Mouliswaran B, Kumar SP, Jeevanantham S, Yaashikaa P (2021) Adsorption characteristics of magnetic nanoparticles coated mixed fungal biomass for toxic Cr (VI) ions in aquatic environment. *Chemosphere* 267:129226

**Publisher's Note** Springer Nature remains neutral with regard to jurisdictional claims in published maps and institutional affiliations.

Springer Nature or its licensor (e.g. a society or other partner) holds exclusive rights to this article under a publishing agreement with the author(s) or other rightsholder(s); author self-archiving of the accepted manuscript version of this article is solely governed by the terms of such publishing agreement and applicable law.